Nanoscale

Accepted Manuscript

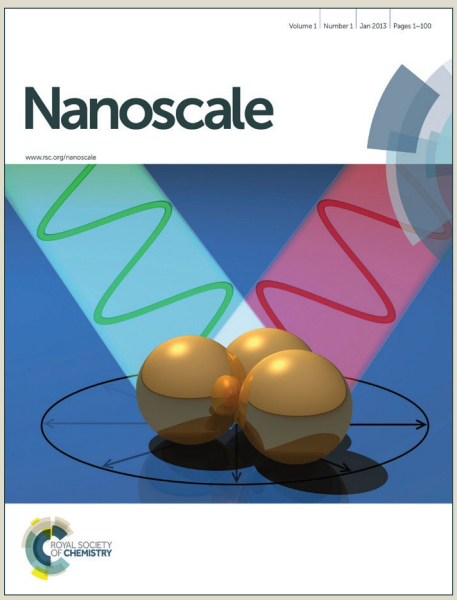

ROYAL SOCIETY OF CHEMISTRY

www.rsc.org/nanoscale

Nanoscale

RSCPublishing

ARTICLE

Crumpled Graphene Nanoreactors

Cite this: DOI: 10.1039/x0xx00000x

Zhongying Wang,[a] Xiaoshu Lv,[b] Yantao Chen,[a] Dan Liu,[a] Xinhua Xu,[b] G. Tayhas R. Palmore,[a c,d] Robert H. Hurt [c,d]

Received 00th January 2012,
Accepted 00th January 2012

DOI: 10.1039/x0xx00000x

www.rsc.org/

Nanoreactors are material structures that provide engineered internal cavities that create unique confined nanoscale environments for chemical reactions. Crumpled graphene nanoparticles or "nanosacks" may serve as nanoreactors when filled with reactive or catalytic particles and engineered for a specific chemical function. This article explores the behavior of crumpled graphene nanoreactors containing nanoscale ZnO, Ag, Ni, Cu, Fe, or TiO_2 particles, either alone or in combination, in a series of case studies designed to reveal their fundamental behaviors. The first case study shows that ZnO nanoparticles undergo rapid dissolution inside the nanoreactor cavity accompanied by diffusive release of soluble products to surrounding aqueous media through the irregular folded shell. This behavior demonstrates the open nature of the sack structure, which facilitates rapid small-molecule exchange between inside and outside that is a requirement for nanoreactor function. In a case study on copper and silver nanoparticles, encapsulation in graphene nanoreactors is shown in some cases to *enhance* their oxidation rate in aqueous media, which is attributed to electron transfer from the metal core to graphene that bypasses surface oxides and allows reduction of molecular oxygen on the high-area graphene shell. Nanoreactors also allow particle-particle electron transfer interactions that are mediated by the connecting conductive graphene, which give rise to novel behaviors such as galvanic protection of Ag nanoparticles in Ag/Ni-filled nanoreactors, and the photochemical control of Ag-ion release in Ag/TiO_2-filled nanoreactors. It is also shown that internal graphene structures within the sacks provide pockets that reduce particle mobility and inhibit particle sintering during thermal treatment. Finally, these novel behaviors are used to suggest and demonstrate several potential applications for graphene nanoreactors in catalysts, controlled release, and environmental remediation.

Introduction

The atomically thin, conformable, and impermeable nature of graphene suggests its use as an outer shell in nano- or micro-encapsulation technologies. Graphene coatings have been explored as protective barriers or selectively permeable films on 2D substrates,[2-5] and they have also been proposed as 3D encapsulants for the immobilization or environmental protection of microscale or nanoscale materials or devices.[6-15] Recently, aerosol microdroplet drying has been demonstrated as an effective method for encapsulating nanoparticle cargos in conductive,[16] electron-transparent, crumpled multilayer graphene shells.[6-9, 11, 17] This process uses graphene oxide sheets of microscale lateral dimension, which assemble through tiling and stacking into quasi-continuous multilayer shells that crumple during the drying process[9].

These crumpled graphene nanosacks have been reported to be open porous structures, rather than perfectly sealed structures,[3] and this may make them poor barriers for protection of the encapsulated material from surrounding fluid environments. The open porosity of crumpled graphene, however, may enable other applications that do not require such barrier protection. For

example, if chemically reactive nanoparticles are encapsulated, the crumpled graphene shell can be regarded as a type of "nanoreactor" that creates an engineered confined nanospace for chemical reactions to occur, and the diffusive transport of small molecules between their interior and exterior should allow the influx of reactants and the out flux of products necessary for reactor function.

In general, a nanoreactor can be defined as a complex material system that has been engineered to host, catalyze, or steer a chemical reaction process occurring in an internal nanoscale cavity. Nanoreactors may host and immobilize chemically active particles, and may alter chemical reaction pathways through confinement effects on transition states or products, by perturbing molecular transport to and/or from the active surfaces, or through electron transfer or other types of interactions between the active particles and the outer shell structure that builds the nano-cavity. The nanoreactor concept has been explored in other material systems, including silica,[18, 19] reverse micelles[20] and proteins with cage-like structures.[21]

The nanoreactor concept has not been systematically developed for graphene-based structures, but the development can be informed by a significant recent literature on crumpled graphene hybrids. Since the first report of crumpled graphene particles in 2011[11], there has been intense interest in their hybridization with active nanoparticles to create composite electrodes, sorbents, and catalysts.[7, 22-28] In these applications, the crumpled graphene serves as a conductive additive and/or support whose folded structure prevents graphene sheet restacking and surface area loss. To support further development, it is important to systematically address the fundamental behaviors of chemical reactions occurring in and on these new material architectures, including the effects of graphene on reactant and product transport, active site accessibility through conformal covering and passivation of internal particle surfaces, as well as particle mobility, stability, sintering, and electron transfer interactions.

Here we synthesize graphene nanosacks filled with nanoparticles of ZnO, Ag, Cu, Ni, Fe, Pt, Pd, and TiO_2 either alone or in combination, as models to explore the fundamental behaviors of crumpled graphene nanoreactors. The filled nanoreactor geometry will be seen to give rise to particle-graphene and particle-graphene-particle interactions that lead to novel reaction behaviors, including enhanced particle oxidation rates, inhibited particle sintering rates, galvanic interactions that affect oxidation and dissolution, and the photochemical control of dissolution and ion release rates. We then use these novel behaviors to demonstrate several example applications of graphene nanoreactors in heterogeneous catalysis, controlled release on antibacterial silver ions, and Fe-mediated reduction of environmental hexavalent chromium.

Experimental

Synthesis of silver stock solution

Citrate-stabilized Ag nanoparticles with average size of 20 nm (Supplementary Information, Fig. S3A) were prepared according to a published method[29] with modification. A 190 mL solution containing 2 mM silver nitrate (Fisher) and 6 mM trisodium citrate (Fisher) was prepared with deionized (DI) water and stirred vigorously at room temperature for 15 min, followed by dropwise addition of 10 ml of 0.12 M $NaBH_4$. After 4 hour stirring at room temperature, the silver nanoparticle stock solution was washed with water and concentrated by centrifugal ultrafiltration (Amicon Ultra-15 3k) and stored at 4 ℃ until further use.

Synthesis of GO and nanoparticle-filled graphene nanosacks

Graphene oxide was synthesized by a modified Hummers method and purified to remove the byproducts, following a previously published procedure.[3, 30] The GO sheets with a nominal size of 1-2 um are primarily in monolayer form, with more complete characterization data can be found in previous publications.[6, 9] Various particle-filled graphene nanosacks were prepared by an aerosol method.[9] Briefly, an ultrasonic nebulizer was used to create a suspended mist from an aqueous suspension of GO (0.5mg/ml) and the target nanoparticle cargo, and carried by nitrogen gas flow through a heated horizontal furnace. The resulting hybrid materials were captured on a PTFE membrane filter (PTU024750, Sterlitech Co.). Most feed suspensions contained nanoparticles (ZnO 1mg/ml commercial NPs from Fisher; Ag: 1mg/ml citrate-stabilized nanoparticles; Ag/TiO_2: 1mg/ml Ag and 0.125mg/ml Evonik P25 grade TiO_2). Cu nanosacks were prepared from Cu(II)-EDTA solution containing 0.5 mg/ml of GO. During the heating process, Cu(II) is reduced to form copper nanoparticles *in situ*. Ag/Cu nanosacks were prepared from a colloid mixture of Ag nanoparticles and Cu(II)-EDTA complex (Ag/Cu mass ratio 2:1) in the presence of

0.5 mg/ml GO. Ag/Ni nanosacks were prepared from a colloid mixture of Ag nanoparticles and Ni nanoparticles from Alfa Aesar (Ag/Ni mass ratio 2:1) in the presence of 0.5 mg/ml GO. In evaluating the effect of Ag/GO ratio on preventing sintering, Ag-rGO nanosacks were prepared from various Ag/GO ratios in the feed suspension. The concentration of Ag and GO is 0.5 mg/ml and 0.5 mg/ml (1:1), 2 mg/ml and 0.5 mg/ml (4:1), 5 mg/ml and 0.5 mg/ml (10:1), 2 mg/ml and 0.05 mg/ml (40:1), respectively.

Electrochemical testing

Electrochemical tests were performed in a CO_2 saturated 0.1M $KHCO_3$ aqueous solution using a conventional H-type two compartment cell separated by a Nafion membrane. The counter electrode was a platinum gauze, and the reference electrode was Ag/AgCl. To prepare the working electrode, Cu/Graphene composite was dispersed in ethanol and drop casted on a carbon paper electrode with a mass density of $2mg/cm^2$.

Preparation of Fe(0) nanosacks and Cr(VI) removal

Fe_3O_4-GO nanosacks were synthesized according to our previous work: 10 mg Fe_3O_4 NPs were mixed with 2mL GO suspension, and then this mixture was diluted to 10 mL. After stirring, ultrasonic were placed to facilitate well dispersion of Fe_3O_4 NPs. Finally, the mixture transferred to the reactor and ultrasonically nebulized into aerosol micro-droplets (feed rate 5 mL/h). Nitrogen gas (0.7 L/min) was purged into the reactor carrying the droplets to pass through a 600 ^oC bench-top electric tube furnace. Synthesized Fe_3O_4-GO nanosacks were collected on the end of the tube by PTFE membrane filter, and these black powders were rinsed by pure alcohol for several times before dried in the oven under 40 ^oC overnight. Empty GO nanosacks were synthesized in the same way from GO suspension. Reduced Fe_3O_4-GO nanosacks (Fe^0-rGO nanosacks) and empty rGO nanosacks were made by reduction of Fe_3O_4-GO nanosacks at 700 ^oC under forming gas (H_2/N_2) for 2 hrs. Bare Fe_3O_4 NPs without GO wrapping were reduced under the same condition to obtain Fe^0 particles for comparison.

Chromium (VI) was chosen as the target pollutant to investigate reactivity of Fe^0-rGO nanosacks and Fe^0 particles made from hydrogen reduction. 2 mg of each synthesized powder (0.2 mg empty GO nanosacks) was added in centrifuge tube, which containing 10 mL potassium dichromate solution (initial concentration of 20 mg/L, pH at 5.0), and the tube was placed on a rotator (60 rpm). Aliquots of the samples were taken at certain time intervals within 2 hrs, and analyzed after being filtered through a 0.22 μm membrane filter. Cr(VI) concentration was determined at 540 nm using a UV-Vis spectrophotometer by the diphenylcarbazine method.

Dissolution Experiments

ZnO nanosacks or agglomerates were incubated in 10 mM $NaNO_3$ solution. After incubating for a predefined time period, the filtrates were separated from the solids using centrifugal ultrafiltration (Amicon ultra-4 3k) for 30 min at 4000 rpm, and were diluted for measurements of zinc by inductively coupled plasma atomic emission spectroscopy (ICP-AES). Silver-based nanosack oxidative dissolution was measured similarly but UV irradiation was involved in fraction of the Ag/TiO_2 samples, and Ag or Cu (in Ag/Cu samples) was measured by graphite furnace atomic absorption spectrometry (Perkin Elmer 4100ZL, GFAAs). All ion release experiments were conducted at room temperature (20℃).

Product Characterization

The morphology and size of nanoparticles or NP-filled nanosacks were determined by transmission electron microscopy (TEM) on a Philips CM20 at 200 kV and scanning electron microscope (SEM) using a LEO 1530 field-emission SEM. The samples were prepared by placing one drop of purified sample solution on carbon-coated copper grids or silicon wafer, followed by drying at room temperature overnight. UV–Vis spectra of 4-nitrophenol sample was recorded on a Jasco V-630 spectrophotometer over the range 300 to 500 nm. The compositions and phases of samples were identified by X-ray diffraction spectrometry (XRD) on a Bruker AXS D8 Advance instrument with Cu Kα radiation (λ = 1.5418 Å). The XRD samples were prepared by adding purified and concentrated suspension onto a glass slide, followed by overnight drying.

Results and Discussion

Nanoreactor synthesis and morphology

Figure 1 shows example morphologies of particle-filled graphene nanosacks synthesized by the in-flight drying of suspended microdroplets. The aerosol process can be carried out with pre-fabricated nanoparticles in the feed suspension (Fig. 1A, B) as reported previously,[8, 9, 26, 31] or using dissolved salt or molecular

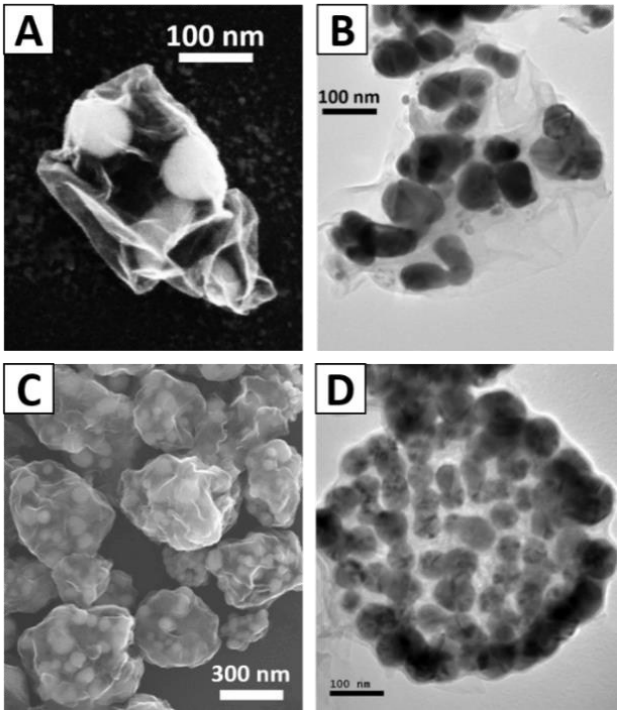

Figure 1. Example morphologies of graphene nanoreactors filled with metallic nanoparticles. (A, B) Ag-filled rGO nanoreactors with a crumpled shell structure fabricated by encapsulation of pre-synthesized Ag-nanoparticles; (C,D) Cu-filled rGO nanoreactors with balloon-like morphology fabricated using a Cu/EDTA complex as a precursor for *in situ* formation of Cu-nanoparticles during the aerosol wrapping process. (A, C are SEM images; B, D TEM images)

precursors that form nanoparticles during the encapsulation process or subsequent annealing.[7] High quality encapsulation requires that the second component be dissolved or stably co-suspended with GO to form a homogeneous two-component feed suspension that segregates into the cargo-sack (core-shell) structure during drying.[6] In the case of particle cargos this homogeneous feed suspension often can be created by tuning the pH so it lies either above or below the isoelectric point of both the GO and particles, giving rise to a repulsive regime where both colloidal materials (particles and GO) have the same surface charge sign and experience electrostatic repulsion in co-suspension.[6] When using salt precursors, the challenge is different - to prevent GO aggregation caused by cation screening of the negative charge on GO, or by GO-cation-GO bridging. Cation-GO binding can cause colloidal instability, but also lead to heterogeneous nucleation of particles on random positions on both sides of the GO sheets, which grow into particles located on both the inside and outside surfaces of the sacks, rather than perfect encapsulation.[7] For this study we developed a technique to avoid these problems with salt precursors using a chelating agent to avoid cation-GO binding. Figure 1C, D shows Cu-filled graphene nanosacks synthesized using $CuCl_2$/EDTA solutions with suspended GO. The addition of EDTA converts the Cu^{2+} to a complex anion with a large stability constant (K_s for Cu-EDTA of $6.3*10^{18}$)[32] that prevents Cu^{2+}-GO association and also introduces a reducing agent for formation of copper nanoparticles[33, 34].

Figure 1C and 1D show the morphology of nanosacks containing zero-valent copper nanoparticles confirmed by XRD (see below), which are successfully encapsulated in graphene with no particles visible on the external surfaces or outside the sack. It is interesting that the Cu-filled nanoreactor structures (Fig. 1C,D) have smoother and more regular surfaces than those made from pre-fabricated Ag particles (Fig. 1A,B). We believe this difference is due to an internal framework from the high Cu particle loadings that limits collapse and crumpling of the graphene, and to gas evolution associated with pyrolytic decomposition of EDTA, which can expand the sack and partially reverse the capillary crumpling that occurs during drying. This chelation method can likely be applied to other salt precursors to allow a range of divalent or trivalent metals at higher concentrations to be used for *in situ* encapsulation. The nanoreactor studies in this paper use filled nanosacks prepared by both methods: particle wrapping, and *in situ* reduction of chelated metal cations, as appropriate.

Particle stability and dissolution

The most fundamental question about crumpled graphene nanoreactors is the extent to which the encapsulated particle surfaces are accessible to external fluid phases, which is a requirement for applications based on catalysis, electrocatalysis, adsorption, or controlled release. To study this phenomenon, we sought a model nanoparticle that is stable enough to survive the fluid-phases aerosol encapsulation process, but also undergoes slow dissolution in aqueous media to release ions that can be quantitatively measured to track dissolution and assess the role of the graphene shell. We chose zinc oxide as the model cargo, which is used extensively in catalysis and sensor applications, as well as in consumer products such as sunscreens and cosmetics. In many of these applications, ZnO dissolution is an important phenomenon that affects stability and durability during use,[35, 36] and also the toxicity and persistence of the ZnO nanoparticles after release to the environment[37-40]. Because of

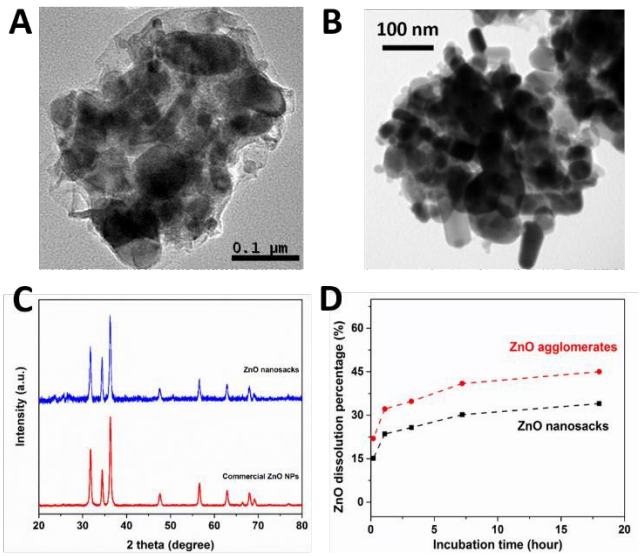

Figure 2. TEM images of (A) ZnO-filled graphene nanosacks and (B) controlled agglomerates of free ZnO nanoparticles, both made by the aerosol drying process; (C) XRD spectra of the free and encapsulated ZnO nanoparticles, showing encapsulation does not alter the phase of ZnO; (D) ZnO dissolution behaviors in 10mM $NaNO_3$, showing that graphene sacks are open and have only a small inhibiting effect on ZnO dissolution rates.

the technological importance of ZnO dissolution, there have been a number of studies that provide dissolution datasets that establish ZnO as a suitable model or reference material for this purpose.

The present work compares the dissolution behavior of free and encapsulated ZnO nanoparticles of similar primary particle size in 10 mM $NaNO_3$ solution (pH 5.8). To control for any changes in the particle phase or surface during the aerosol encapsulation process, and to control for aggregation effects, we prepared controlled agglomerates of ZnO nanoparticles by repeating the aerosol droplet drying process but in the absence of graphene oxide. The result is a set of equi-axed ZnO agglomerates (Fig. 2B) of similar size and shape to the graphene-ZnO nanosacks (Fig. 2A). XRD spectra (Fig. 2C) indicate the aerosol encapsulation process did not alter the composition or phase of ZnO.

Figure 2D shows the rapid dissolution of free ZnO agglomerates within 20 hours in agreement with Ma et al.[40] The ZnO particles inside crumpled graphene sacks show a similar time scale for dissolution, but with an offset in the total amount dissolved that may be caused by adsorption of Zn^{2+} on polar functional groups on rGO,[41] or by some small fraction of deeply imbedded ZnO. For both samples, the concentration of dissolved Zn reaches an apparent equilibrium after 20 hours. Based on calculations performed using the aqueous-phase thermodynamics package *Visual Minteq*[42] the equilibration is not due to formation of $Zn(OH)_2$, but instead is caused by an increase in pH from 5.8 to 6.7, which we measured over the course of the dissolution process. Overall, these results show that encapsulation in graphene nanosacks does not protect ZnO nanoparticles from dissolution. Neither transport limitations on exiting Zn-ions nor the coverage of particle surfaces by graphene sheets have a major effect on the initial rate of dissolution of ZnO. The lack of transport limitations is consistent with reaction (dissolution) times that are much longer than characteristic diffusion times, L^2/D, which are estimated to be ~10 usec (for 100 nm length scale, 10^{-5} cm^2/s diffusivity). The lack of a large wrapping inhibition effect is consistent with the nanoscale size of the particles, whose surface curvature is far too great to allow large-area conformal contact coverage by graphene microsheets. Such coverage would require high Gaussian (2D) curvature that would cause sheet buckling that prevents large-area conformal contact. This ZnO case study deals with a simple dissolution process, involving only fluid access but no oxidation or electron transfer. Quite different behaviors are seen in the next section on oxidation-driven dissolution processes.

Anomalous enhancement of particle oxidation

Many nanomaterials are stable to dissolution in their current oxidation states, but in the presence of O_2 undergo oxidation with release of soluble ions or complexes.[29, 43, 44] This oxidative dissolution has been shown to be important in the biological and environmental behavior of nanoscale Ag, [29, 44, 45] Cu,[43, 46] Ni[47] and Fe,[48, 49] where it determines the concentration of the soluble ionic species that can be the primary toxic species in particle-containing suspensions.[43, 45, 48] The present article reports the surprising finding that encapsulation in graphene sacks *increases* the rate of oxidation of nanoscale Cu and Ag despite the introduction of an apparent physical barrier to oxygen access.

We tracked the appearance of soluble copper and silver ions during the incubation of the crumpled rGO hybrids and free metal nanoparticles. Figure 3 shows their dissolution rates in acetate buffer (pH 5.7). The Cu dissolution rate is extraordinarily fast within the crumpled graphene nanoreactors, a result that can be directly observed in the form of Cu-depleted reactor structures after incubation for only one hour (Fig. 3C). The encapsulated and free particles have a similar size and crystal phase (Fig. 3A and

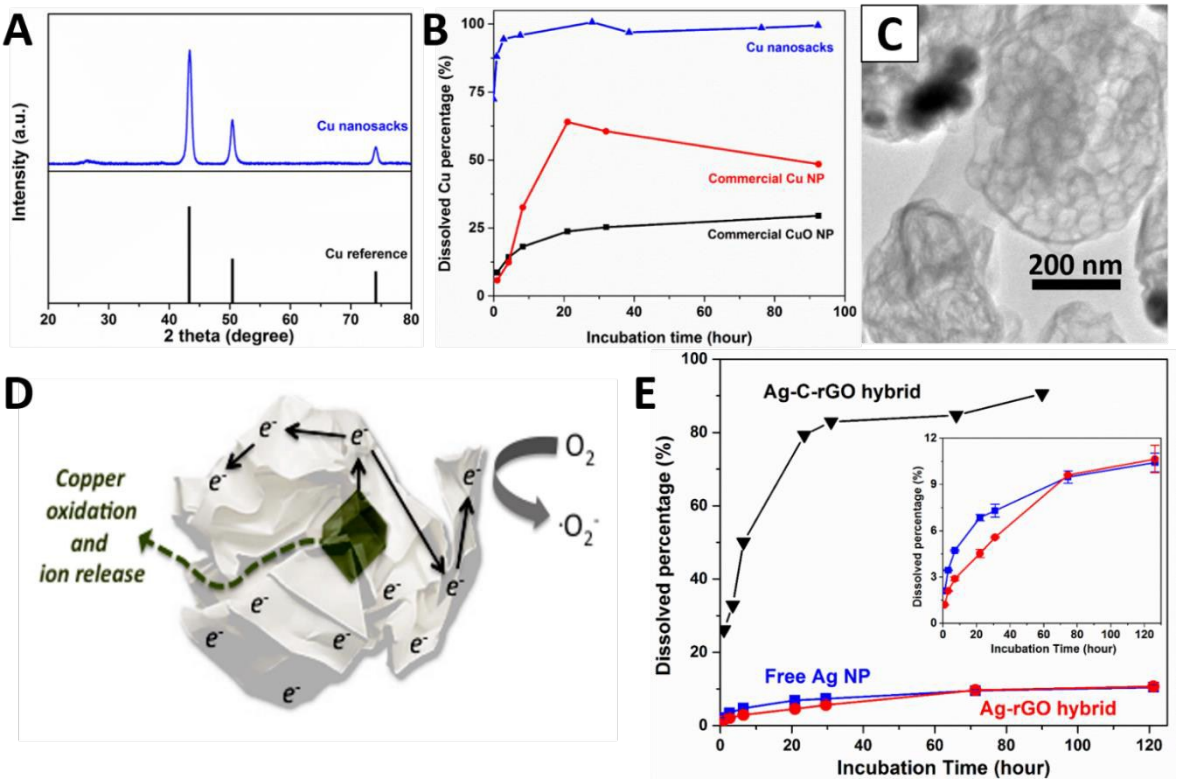

Figure 3. Nanoparticle oxidation is accelerated inside graphene nanoreactors in some cases. (A) XRD spectra of copper nanoparticles within graphene nanosacks. (B) Time-dependent dissolution behavior of copper in rGO-Cu nanosacks and commercial Cu nanoparticles in acetate buffer. Note that the decrease of dissolved Cu seen in the Cu NP sample after 20 hours is due to the comproportionation of Cu nanoparticles and dissolved Cu^{2+} to form the insoluble Cu_2O shell.[1] (C) TEM image of rGO-Cu nanosacks after one-hour incubation in acetate buffer showing the depletion of Cu-NPs with intact sack structure. Note the internal spherical structures, which are EDTA-derived carbon shells at the locations of the original Cu-NP surfaces. (D) Mechanism of electron transfer to rGO and Cu-ion release by diffusion through the irregular pore structure of the folded structure. (E) Similar effect seen in the Ag-graphene system when EDTA is used as an additive to create carbon shells around the particles (Ag-C-rGO hybrid), but not in the presence of the rGO sack alone as the only carbon component (Ag-rGO hybrid).

Supplementary Information, Fig. S1), so the effect must be related to the hybridization of the particles with carbon. Recent studies on graphene-coated planar substrates suggest that electron transfer from the metal to graphene can promote metal oxidation by providing a conductive pathway from the unoxidized metal core to the external oxidant that bypasses an insulating oxide shell.[50, 51] For nano-Cu, it is known that a solid oxide film forms during the oxidative dissolution process,[46] and electron transfer through an insulating Cu_2O film has been proposed as the rate-limiting step in Cu corrosion.[51] Within the nanoreactor, the metallic particles are in direct contact with internal carbon structures that include multilayer rGO sheets and near-spherical carbon shells formed by EDTA pyrolytic decomposition, which are easily seen in Fig. 3C. Copper is well known to transfer electrons to graphene to equilibrate the Fermi levels,[52, 53] and we propose that Cu transfers electrons to these internal carbon structures and spreads them to the high-area outer surface where they participate in oxygen reduction.[54, 55] Facile electron transport through conductive rGO replaces slower electron transport through Cu_2O and thus accelerates the reaction. In addition, reduced oxygen species formed through electron transfer to dissolved O_2 are generated primarily at the surface of the graphene sack and not the surface of Cu, and as such, are not readily available to facilitate formation of Cu-oxide. This physical separation of newly formed oxide species from copper may limit the formation of surface oxide and instead favor direct Cu-cation release. When electron transfer through graphene is coupled with diffusion of soluble Cu ions through the porous, water-filled sack structure (see above), the result is a complete redox process with the net effect of accelerating nanoparticle oxidation (Fig. 3D).

Figure 3E shows that this enhancement also can be observed in the silver-graphene system in some cases. Oxidative dissolution of silver nanoparticles have been extensively studied,[29, 56-58] and is seen here to be accelerated when Ag particles are formed within crumpled rGO using EDTA as an additive (see "Ag-C-rGO hybrid" curve). Interestingly, if pre-fabricated Ag particles are encapsulated without the use of EDTA, the rGO sack alone has little effect on dissolution (see "Ag-rGO hybrid" curve). This suggests that the EDTA-derived carbon shells ("C" in "Ag-C-rGO hybrids") are the primary feature that enhances corrosion by promoting electron transport through or around the surface metal oxide layers due to their intimate contact with the particle surfaces and connection to the outer graphene shell (Fig. 3C). Finally we also used these same methods to create Pt- and Pd-filled nanosacks (structures in Fig. S5), but oxidative dissolution of these metals was too slow to be used as a diagnostic for the effect of graphene encapsulation. Together these results show that crumpled graphene reactor shells allow ready access of external fluid phases to internal particles surfaces, and show only slight inhibitory effects on simple dissolution processes (e.g. ZnO). The crumpled graphene shell also has little effect on oxidative dissolution processes, but the highly conformal EDTA-derived carbon shells in intimate contact with metal surfaces can promote electron transport and have a strong enhancing effect on the oxidative corrosion of both Ag and Cu nanoparticles.

Inner-space catalysis

There is great interest in graphene-particle hybrids as advanced architectures for heterogeneous catalysis and electrocatalysis.[59-63] The internal spaces in graphene sack nanoreactors are accessible to small molecule solutes (Fig. 2, 3), but the ability of these filled nanoreactors to serve as functioning catalytic systems is unclear. As a simple test of catalytic activity, we used Cu-NPs and Ag-NPs in nanoreactor environments for electrochemical reduction of CO_2 and 4-nitrophenol reduction, respectively. Copper is known to be one of the most effective metallic catalysts for carbon dioxide electroreduction.[64-66] Fig. 4A shows cyclic voltammograms of rGO-Cu sacks in 0.1 M aqueous $KHCO_3$ sparged with 1 bar CO_2 gas. The lower onset potential and higher current density of this graphene-particle hybrid relative to the carbon paper control demonstrates the catalytic activity of the rGO-Cu nanosacks. It is noteworthy that the nanosacks give a lower onset potential for CO_2 electroreduction than pure Cu foil (Fig. 4A). The current per superficial electrode area is similar for the nanoreactors and the Cu-foil (main figure), but the current on the basis of equal Cu mass is much higher for the graphene-Cu nanoreactor sample (Fig. 4A inset). Energy dispersive X-ray spectroscopy (EDX) and Grazing Incidence X-ray Diffraction (GI-XRD) results (Supplementary Information, Fig. S2) show that Cu remains in the metallic phase during these cycles.

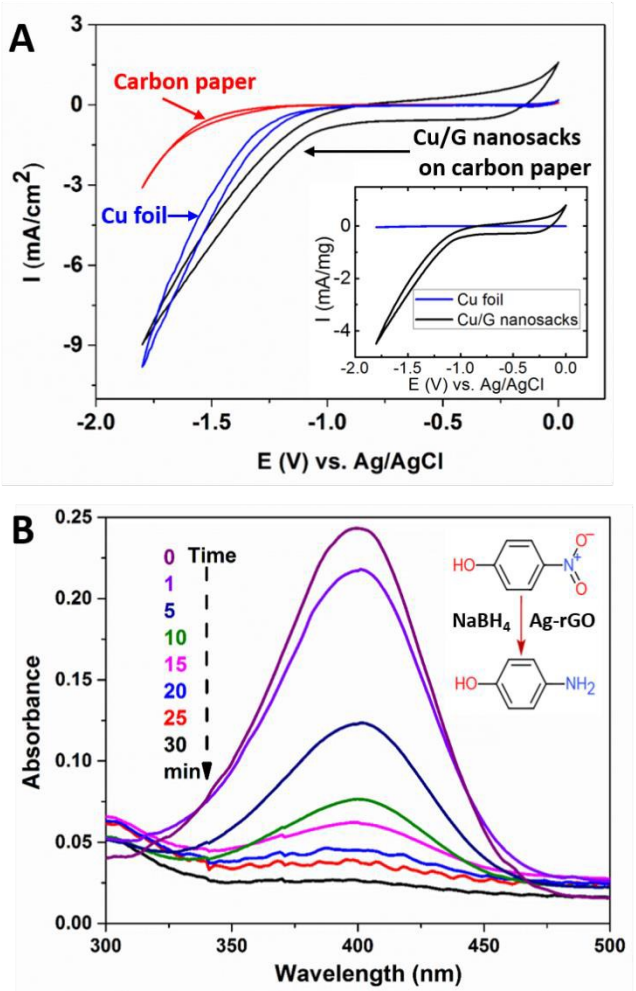

Figure 4. Catalytic activity of Cu and Ag nanoparticles when encapsulated in graphene nanosacks. (A) Cyclic voltammogram showing activity of rGO-Cu nanoreactors for the electrochemical reduction of CO_2 in 0.1 M aqueous $KHCO_3$. The inset plot shows current of the Cu-foil and graphene-nCu hybrid normalized by copper mass, showing the much higher activity of the graphene-nCu system. (B) Time dependent adsorption spectra of 4-nitrophenol showing its depletion by borohydride reduction catalyzed by rGO-Ag nanoreactors.

For a non-electrochemical reaction, we used Ag-catalyzed reduction of 4-nitrophenol (Nip) to aminophenol as a model reaction (inset of Fig. 4B). The reduction of Nip by borohydride is catalyzed on Ag and Au surfaces, and this catalytic reaction has often been used as a model to benchmark the activity of nanoparticle catalyst formulations.[67-69] Here, the characteristic UV-vis adsorption peak of Nip at 400 nm is used to monitor this reaction in the presence of rGO-Ag nanosacks. Ag nanosacks (1mg/mL, 2μL) were added to a 1 mL solution containing Nip (1.4×10^{-4} M) and $NaBH_4$ (4.2×10^{-2} M), and Fig. 4B shows the Nip depletion dynamics in the presence of the rGO-Ag nanoreactors, which demonstrates rGO-Ag nanosacks are catalytically active. For comparison, Ag catalyst prepared by the same aerosol process without graphene wrapping was also used in the nitrophenol reduction reaction at the same mass of Ag-rGO nanosacks, but showed no activity. The Nip reduction rate is expected to be proportional to the amount of Ag surface available for surface hydride formation (by BH_4^-) Nip adsorption, surface reaction, and desorption, according to the accepted mechanism for catalytic Nip reduction.[70] Without graphene wrapping, the loss of Ag activity is due to thermal sintering at 600℃ (*vida infra*). The role of graphene nanoreactors in sintering inhibition is explored in more detail in the following section.

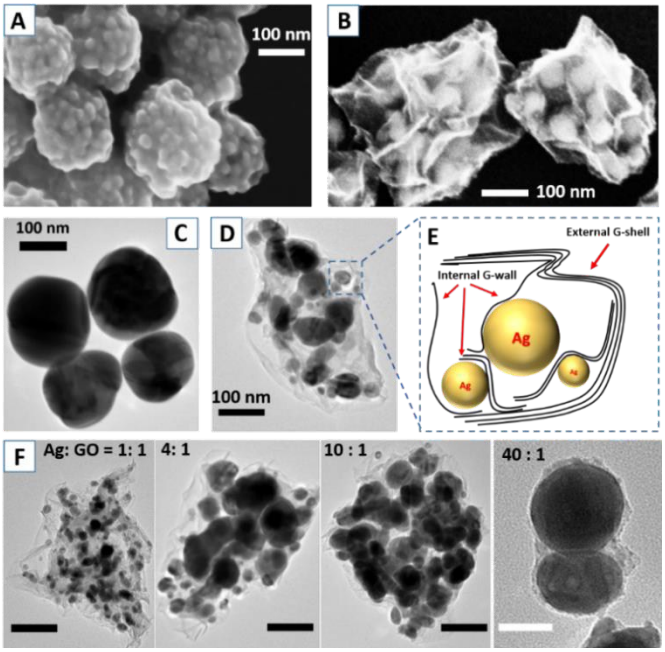

Figure 5. Sintering inhibition of nanoparticles within crumpled graphene nanoreactors. (A, B) Final Ag particle structures after rapid thermal treatment in flight at 400 ℃ in N_2 gas during the aerosol process: (A) controlled Ag agglomerates with no graphene, (B) Ag-NPs inside crumpled graphene nanoreactors. (C, D) Final Ag particle structures after rapid thermal treatment in flight at 600 ℃ in N_2 gas during the aerosol process: (C) controlled Ag agglomerates with no graphene, (D) Ag-NPs inside crumpled graphene nanoreactors. (E) Sketch of internal graphene structures that are proposed to prevent particle-particle interactions and release, while allowing small molecule solutes access to active surfaces. (F) Sintering inhibition is more effective at high GO:Ag ratio. TEM images of sintered Ag in graphene nanoreactors treated at 600 ℃ at different Ag:GO ratios (left to right): 1, 4, 10, 40. The black scale bar represents 100 nm, while the white scale bar represents 50 nm.

Sintering inhibition

Among the desired functions of a catalyst support is to enhance and maintain particle dispersion and active surface area. Both particle mobility and atomic mobility at particle surfaces can cause a loss in surface area and catalytic activity under reaction conditions at elevated temperatures. We found the crumpled graphene nanoreactor architecture to be effective at suppressing particle-particle interactions and thermal sintering. Figure 5 compares the behavior of free and encapsulated Ag nanoparticles heated at 400 ℃ (A, B) and 600 ℃ (C, D) in inert gas. Controlled Ag-NP agglomerates were made by nebulization of Ag-NP suspensions and *in situ* drying, and in the absence of graphene, these agglomerates undergo rapid partial fusion at temperatures as low as 400 ℃ (Fig. 5A). At 600 ℃ one large rounded Ag particle forms from the complete fusion of the initial agglomerate (Fig. 5C). The addition of graphene, however, maintains the initial particle structure at both temperatures during the aerosol process (Fig. 5B, D), which we believe is due to physical restriction of particle motion by internal graphene structures. Sintering suppression is characteristic of crumpled graphene nanoreactors, whose folded structures create internal nanoscale pockets for the particles that serve as physical barriers to particle mobility or release (Fig. 5E), but whose characteristic pore sizes around 4 nm[6, 9] allows small molecule reactants (< 4 nm) access to catalyst active sites.

Figure 5F shows that the sintering inhibition depends on the relative amounts of Ag and graphene in the filled reactor structures. As the initial Ag/GO mass ratio increases from 1 to 40, the ability of internal graphene structures to inhibit sintering declines. We believe that high graphene content produces more

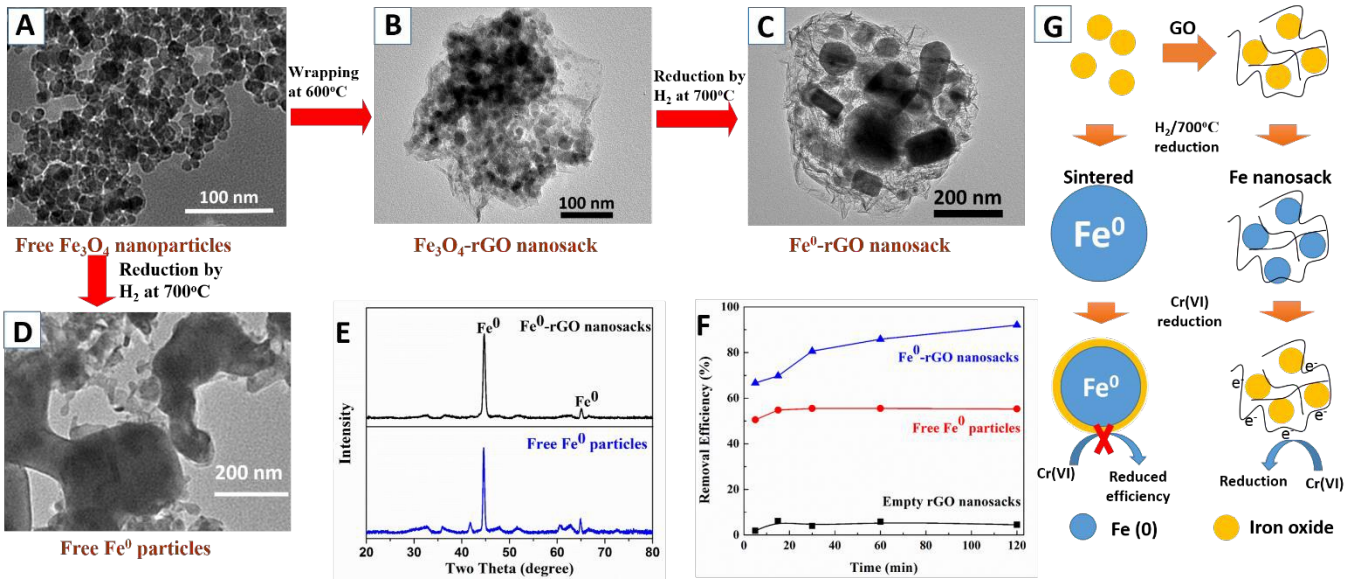

Figure 6. Use of graphene nanoreactors to increase the activity of Fe^0-NPs for environmental reduction of Cr(VI). TEM images of (A) free Fe_3O_4 NPs; (B) Fe_3O_4-filled nanoreactors; (C) Fe^0-filled nanoreactors (See Fig. S4 for SEM); (D) free Fe^0 particles. (E) XRD spectra of Fe^0-filled nanoreactors and free Fe^0 particles. (F) Comparison of Cr(VI) removal efficiency within 2 hrs. Note: the graphene-only control shows the main activity for Cr(VI) removal is associated with the iron phases. (G) Proposed mechanism.

internal compartments and fewer Ag-NPs per compartment, leading to smaller final particles after thermal treatment. To test sintering inhibition at longer times, we treated pre-fabricated Ag-filled nanoreactors to temperatures ranging from 500-700 ℃ for one hour in a horizontal tube furnace. The Ag nanoparticles were stable inside graphene nanoreactors for one hour at 500 ℃ in N_2 and at 700℃ in 5/95% H_2/N_2 (Supplementary Information, Fig. S3B, D). Interestingly, the graphene nanoreactors were destroyed and the Ag-NPs fully sintered at 700 ℃ in the absence of H_2 (Supplementary Information, Fig. S3C), which is likely due to trace oxygen in the N_2 annealing gas environment. The crumpled graphene shells here are composed of only about 10 atomic layers,[9] and it is not surprising that they are easily gasified by exposure to trace oxygen at 700℃, which is above the typical initiation temperature for rGO oxidation by air.

The graphene nanoreactor architecture also can be used to increase the reactivity of nano-zero-valent iron (nZVI) for the environmental remediation of Cr(VI) through chemical reduction. One route to nZVI is reduction of Fe_3O_4 nanoparticles with low Cr(VI) removal efficiency, (Supplementary Information, Fig. S6) but sintering or aggregation at the high-temperatures employed reduces the activity of the nZVI.[71, 72] Surface coatings based on silica[73] or carbon[74] have been explored to maintain the iron oxide nanostructure during reduction. Figure 6 compares the reductive activity of derived nZVI prepared from Fe_3O_4 particles in the free state and imbedded in graphene nanoreactors. The free particles undergo significant sintering and area loss during the 700 ℃ hydrogen reduction step (A→D), while the encapsulated particles show better size and area retention (B→C). Though Fe as free particles and within nanoreactors have the same composition and phase (Fig. 6E), the nZVI particles within the nanoreactors are more effective at Cr(VI) reduction (Fig. 6F). The initial kinetics are fast in both cases, but the free iron particles lose activity at just over 50% conversion while Fe^0-filled graphene nanoreactors retain activity through the complete elimination of Cr(VI). Note that rGO nanosacks alone at the same mass loading showed very limited adsorption/reduction of Cr(VI), so the effects observed relate to differences in the activity of the iron phases. We believe the improved performance of the nanoreactor sample is the result of two effects: (i) encapsulation inhibits sintering during synthesis and yields smaller particles with higher external area, and (ii) electron transfer between Fe^0 and graphene allows indirect reduction of Cr(VI) by Fe^0 at the sack surface and prevents the formation of a passivating oxide film at local points of particle-graphene contact.

This enhanced reductive activity toward Cr(VI) is analogous to the enhanced reductive activity toward O_2 observed for Cu-rGO nanosacks that leads to fast Cu dissolution (above).

Complex nanoreactors: photochemical control of Ag-ion release

The data in Figs. 2-6 have shown novel behaviors that arise from particle-graphene interactions in the nanoreactor architecture. Even more complex behaviors emerge when multiple particle types are introduced into the graphene nanoreactor interior. Figure 7 for example shows the controlled Ag dissolution behavior in ternary Ag/TiO_2-rGO nanosacks in aqueous suspension in the presence and absence of UV illumination. Ion release is a key process that governs the antibacterial activity of silver nanoparticles, because the Ag^+ ion is the primary toxic species to bacteria. There is great interest in methods to control this release in order to deliver the toxic ion at the correct dose to the correct target and at the correct time, thus maximizing the effectiveness of nanosilver and reducing the total amount of nanosilver required in a given consumer or medical application.[44, 45, 75-78] As a measure of the rate of oxidation of nano-Ag, the time evolution of dissolved silver concentration was monitored by graphite furnace atomic absorption spectroscopy after nanosack removal by ultrafiltration.[29] The rate of oxidative dissolution of nano-Ag in the dark is similar to that reported previously,[29, 79, 80] but the release is completely suppressed during UV illumination (Fig. 7B). Oxidative dissolution restarts immediately when the UV lamp is switched off, and when the lamp is turned back on the accumulated Ag^+ undergoes active reduction lowering silver ion concentration (Fig. 7B). This demonstrates active control of Ag-ion release and re-reduction using three-component graphene nanosacks.

Some aspects of this behavior are readily understood from the existing literature. Titania is an active photocatalyst, but when present as isolated particles, electron-hole recombination can limit its efficiency.[59, 81] Hybridizing TiO_2 with graphene has been reported in multiple studies to increase photoefficiency by electron transport and spreading onto the 2D carbon sheet, which promotes electron-hole separation and inhibits recombination.[81, 82] Furthermore, high efficiencies in Ag-TiO_2-graphene systems have been reported through graphene (rGO) transport of excited electrons for Ag reduction, though the effect on Ag transformations was not studied. Silver ion reduction also has been reported on illuminated TiO_2 surfaces.[83] The data shown in Fig. 7C reveals a behavior unique to Ag/TiO_2-rGO nanoreactors. The Ag^+ ion release is suppressed by trace amounts of TiO_2 (1% of the Ag loading). This amount of TiO_2 is not effective when present as free particles in suspension with nano-Ag (Fig. 7C). We propose that the highly sensitive control of Ag-ion release in Ag/TiO_2-rGO nanoreactors is due to the enhancement of TiO_2 photoreactivity by direct electron transfer through graphene to silver[81] combined with the elevated concentration of the Ag and TiO_2 components that are concentrated in the reactor interior. Any silver ion produced through nano-Ag oxidation must encounter electron-doped graphene structures before diffusion through the porous sack, and the internal reduction process is too fast to allow measurable release (Fig. 7D). Photo-controlled release and capture of silver ions shown by Ag/TiO_2-rGO nanosacks is unique and may have potential in controlled release antibacterial or other delivery applications.

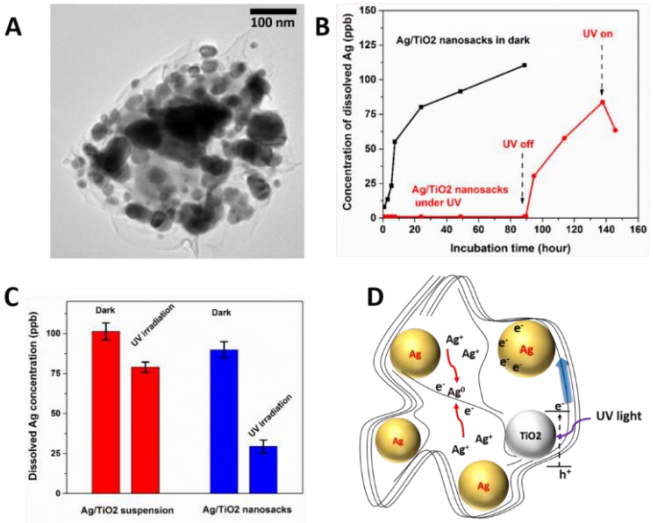

Figure 7. Complex nanoreactors: photochemical control of Ag-ion release. (A) TEM image of Ag/TiO_2-rGO nanosacks; (B) Time-resolved measurement of Ag ion release from Ag/TiO_2-rGO nanosacks in dark or under UV irradiation; (C) Ag ion release from Ag/TiO_2-rGO nanosacks with small amounts of TiO_2 in dark or UV irradiation incubated for one day. Here the oxidation protection provided by TiO_2 is much more effective in the nanoreactor configuration than from free Ag and TiO_2 in suspension under the same conditions; (D) Proposed mechanism for suppression of Ag oxidation by electron transfer and active Ag^+ reduction on graphene surfaces.

Complex nanoreactors: galvanic control of Ag-ion release

Another emergent behavior of three-component nanoreactors involves galvanic interactions between dissimilar imbedded metals. "Galvanic control" of Ag-ion release is defined as the use of a less noble metal, in addition to Ag and in electrical contact with Ag, as a sacrificial agent that preferentially oxidizes and thus delays Ag

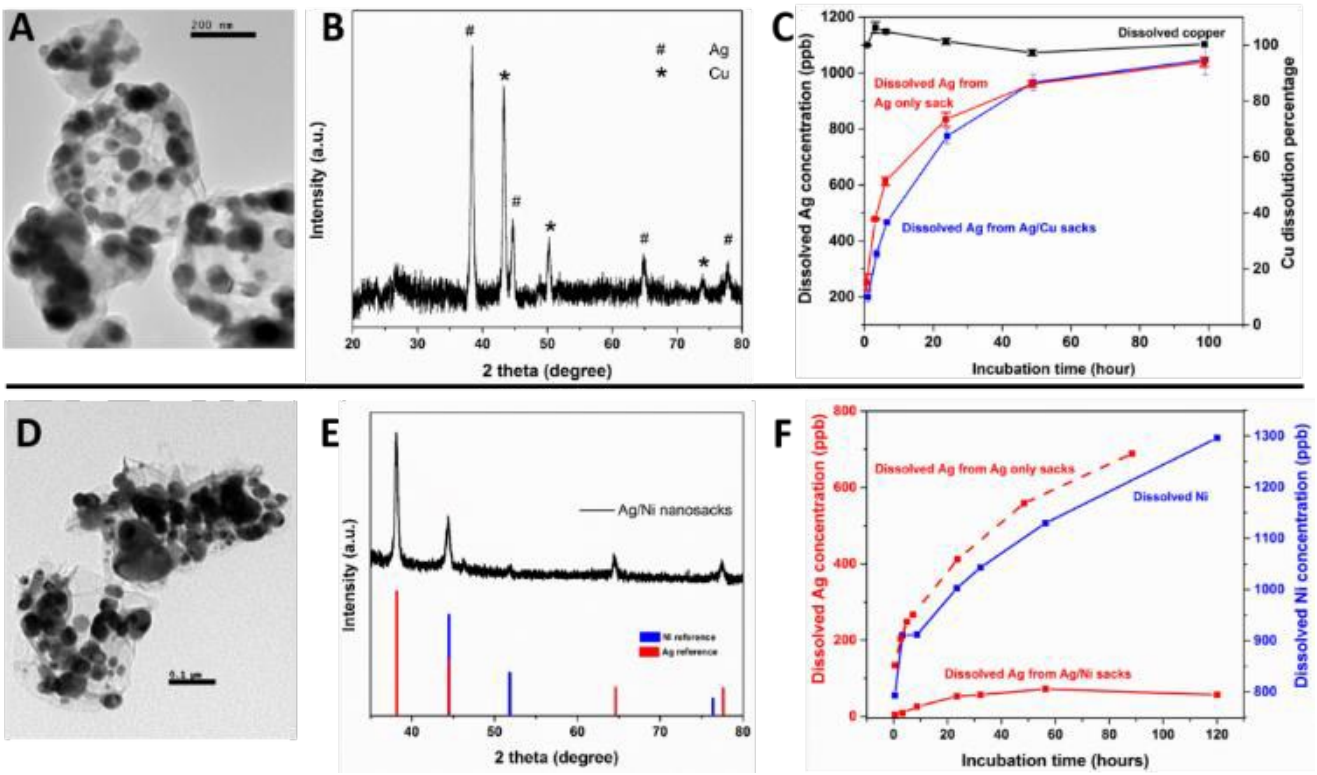

Figure 8. Complex nanoreactors: galvanic control of Ag-ion release. (A-C) Ag/Cu-rGO nanosacks, (A) morphology by TEM, (B) phases by XRD, and (C) oxidative dissolution behavior for both Ag (total Ag concentration is 3 ppm) and Cu components in acetate buffer. Cu oxidation and dissolution is rapid, and does not alter the oxidative dissolution profile of nano-Ag observed when present alone in Ag-rGO nanosacks. (D-F) Ag/Ni-rGO nanosacks, (D) Morphology by TEM, (E) phases by XRD, (F) oxidative dissolution behavior of both Ag and Ni components in acetate buffer.

oxidation and Ag ion release for a prescribed time. We explored the addition of a less noble metal to Ag-rGO nanoreactors as a non-photochemical method to control Ag-ion release. Figure 8 shows the behavior for Cu (A-C) and Ni (D-F) introduced as the less noble metal. The Ag/Cu-rGO reactors (A-C) were prepared by the aerosolization of GO with the dissolved Cu-EDTA complex described in Fig. 1. For a better comparison, the Ag-rGO nanoreactors were made from pre-synthesized particles as in Fig. 1, but also with the addition of EDTA that may affect the ion release rates.

Figure 8C shows the time-dependent dissolution behavior for both elements. The dissolution of Cu is fast, as observed previously for the simple Cu-rGO system (see Fig. 2), and the Ag oxidative dissolution is unaffected by addition of copper. The inability of Cu to influence Ag-ion release is easily understood – Cu oxidation and dissolution is rapid enough that the Cu-NPs are not present for most of the time period of Ag oxidation. The mismatch between Ag and Cu oxidation kinetics prevents Cu from being effective as a method for galvanic control of Ag-ion release.

A different behavior is seen in the case with nickel. Figure 8D-F show the behavior of Ag/Ni-rGO nanoreactors. The similar rates of oxidative dissolution for free silver and encapsulated Ni allow Ni to strongly suppress Ag-ion release. This suppression can be the result of a galvanic replacement reaction (e.g. $2Ag^{+} + Ni \rightarrow 2Ag + Ni^{2+}$) or by electron transfer from Ni through rGO to Ag, providing cathodic protection that prevents Ag oxidation. The use of the sacrificial metal introduces an induction period before Ag ion release begins, and we expect the induction period to be controllable by varying the sacrificial metal mass loading, with potential applications where extended release is needed in consumer products or medical devices.

Conclusions

Crumpling graphene around chemically reactive or catalytic particles can lead to "nanoreactor" systems with active internal cavities that can be exploited for the engineering of chemical reactions. The crumpled structure can be designed to immobilize and retain the active nanoparticles, while providing diffusional pathways through < 4 nm pores for small molecule reactants and products to enter and exit the internal nanocavity during reaction. This paper explores nanoreactor behaviors using ZnO, Cu, Ag, Ni, Fe, and TiO_2 nanoparticles as model fillers. We show that the complex 3D crumpled structure and electrical conductivity of the graphene shell gives rise to novel behavior that includes (i) inhibition of particle sintering (Ag, Fe), (ii) enhancement of particle oxidation (Cu, Ag) in some cases where internal conformal carbon shells are present, (iii) cathodic protection against oxidation (Ag) using a co-imbedded sacrificial particle (Ni), (iv) TiO_2-mediated photochemical control of silver ion release, (v) and enhanced performance in the Fe-based reduction of environmental Cr(VI). These novel behaviors coupled with the continuous fabrication method and the flexible ability to fill the graphene shells with one or multiple types of chemically reactive or catalytic particles, make crumpled graphene nanoreactors attractive for a variety of applications in catalysis, electrocatalysis, controlled release, and environmental nanotechnology.[84]

Acknowledgements

The authors acknowledge financial support from the U.S. National Science Foundation through the Brown-Yale Center for the Capture and Conversion of CO_2 (C4), NSF Award CHE-1240020.

Notes and references

[a] Department of Chemistry, Brown University, Providence, Rhode Island 02912, United States
[b] Department of Environmental Engineering, Zhejiang University, Hangzhou 310058, People's Republic of China.
[c] School of Engineering, Brown University, Providence, Rhode Island 02912, United States
[d] Institute for Molecular and Nanoscale Innovation, Brown University, Providence, Rhode Island 02912, United States

Electronic Supplementary Information (ESI) available: Figure S1-S5. See DOI: 10.1039/b000000x/

1. F. Wen, C. Xie, X. Xia and G. Le, *J. Electroanal. Chem.*, 2007, **603**, 219-226.
2. A. K. Geim and I. V. Grigorieva, *Nature*, 2013, **499**, 419-425.
3. F. Guo, G. Silverberg, S. Bowers, S.-P. Kim, D. Datta, V. Shenoy and R. H. Hurt, *Environ. Sci. Technol.*, 2012, **46**, 7717-7724.
4. Y. Su, V. G. Kravets, S. L. Wong, J. Waters, A. K. Geim and R. R. Nair, *Nat Commun*, 2014, **5**.
5. V. Berry, *Carbon*, **2013**, **62**, 1-10.
6. Y. Chen, F. Guo, Y. Qiu, H. Hu, I. Kulaots, E. Walsh and R. H. Hurt, *ACS Nano*, 2013, **7**, 3744-3753.
7. S. Mao, Z. Wen, H. Kim, G. Lu, P. Hurley and J. Chen, *ACS Nano*, 2012, **6**, 7505-7513.
8. J. Luo, X. Zhao, J. Wu, H. D. Jang, H. H. Kung and J. Huang, *J. Phys. Chem. Lett.*, 2012, **3**, 1824-1829.
9. Y. Chen, F. Guo, A. Jachak, S.-P. Kim, D. Datta, J. Liu, I. Kulaots, C. Vaslet, H. D. Jang, J. Huang, A. Kane, V. B. Shenoy and R. H. Hurt, *Nano Lett.*, 2012, **12**, 1996-2002.
10. X. Ma, M. R. Zachariah and C. D. Zangmeister, *Nano Lett.*, 2011, **12**, 486-489.
11. J. Luo, H. D. Jang, T. Sun, L. Xiao, Z. He, A. P. Katsoulidis, M. G. Kanatzidis, J. M. Gibson and J. Huang, *ACS Nano*, 2011, **5**, 8943-8949.
12. T. Cassagneau and J. H. Fendler, *J. Phys. Chem. B*, 1999, **103**, 1789-1793.
13. W. Zhou, J. Zhu, C. Cheng, J. Liu, H. Yang, C. Cong, C. Guan, X. Jia, H. J. Fan, Q. Yan, C. M. Li and T. Yu, *Energy Environ. Sci.*, 2011, **4**, 4954-4961.
14. M. Zhu, P. Chen and M. Liu, *ACS Nano*, 2011, **5**, 4529-4536.
15. S. Yang, X. Feng, S. Ivanovici and K. Müllen, *Angew. Chem., Int. Ed.*, 2010, **49**, 8408-8411.
16. S. M. Tan, A. Ambrosi, C. K. Chua and M. Pumera, *J. Mater. Chem. A*, 2014, **2**, 10668-10675.
17. J. Luo, H. D. Jang and J. Huang, *ACS Nano*, 2013, **7**, 1464-1471.
18. J. Zong, Y. Zhu, X. Yang, J. Shen and C. Li, *Chem. Commun. (Cambridge, U. K.)*, 2011, **47**, 764-766.
19. J. Liu, S. Z. Qiao, S. Budi Hartono and G. Q. Lu, *Angew. Chem., Int. Ed.*, 2010, **49**, 4981-4985.

20. Y. Lee, J. Lee, C. J. Bae, J. G. Park, H. J. Noh, J. H. Park and T. Hyeon, *Adv. Funct. Mater.*, 2005, **15**, 503-509.

21. C. Sun, H. Yang, Y. Yuan, X. Tian, L. Wang, Y. Guo, L. Xu, J. Lei, N. Gao, G. J. Anderson, X.-J. Liang, C. Chen, Y. Zhao and G. Nie, *J. Am. Chem. Soc.*, 2011, **133**, 8617-8624.

22. W.-N. Wang, Y. Jiang, J. D. Fortner and P. Biswas, *Environ. Eng. Sci.*, 2014, **31**, 428-434.

23. A. J. Smith, Y.-H. Chang, K. Raidongia, T.-Y. Chen, L.-J. Li and J. Huang, *Advanced Energy Materials*, 2014, **4**, n/a-n/a.

24. S. Mao, Z. Wen, T. Huang, Y. Hou and J. Chen, *Energy & Environmental Science*, 2014, **7**, 609-616.

25. S. Mao, Z. Wen, Z. Bo, J. Chang, X. Huang and J. Chen, *ACS Appl. Mater. Interfaces*, 2014.

26. Y. Jiang, W.-N. Wang, P. Biswas and J. D. Fortner, *ACS Appl. Mater. Interfaces*, 2014, **6**, 11766-11774.

27. X. Chen, G. Wu, T. Lan and W. Chen, *Chem. Commun. (Cambridge, U. K.)*, 2014, **50**, 7157-7159.

28. H. D. Jang, S. K. Kim, H. Chang, J.-W. Choi, J. Luo and J. Huang, *Aerosol Sci. Technol.*, 2013, **47**, 93-98.

29. J. Liu and R. H. Hurt, *Environ. Sci. Technol.*, 2010, **44**, 2169-2175.

30. F. Kim, J. Luo, R. Cruz-Silva, L. J. Cote, K. Sohn and J. Huang, *Adv. Funct. Mater.*, 2010, **20**, 2867-2873.

31. X. Jia, Y. Cheng, Y. Lu and F. Wei, *ACS Nano*, 2014, **8**, 9265-9273.

32. D. W. Choi, C. J. Zea, Y. S. Do, J. D. Semrau, W. E. Antholine, M. S. Hargrove, N. L. Pohl, E. S. Boyd, G. G. Geesey, S. C. Hartsel, P. H. Shafe, M. T. McEllistrem, C. J. Kisting, D. Campbell, V. Rao, A. M. de la Mora and A. A. DiSpirito, *Biochemistry*, 2006, **45**, 1442-1453.

33. E. Escrivá, A. Fuertes, J. V. Folgado, E. Martínez-Tamayo, A. Beltrán-Porter and D. Beltrán-Porter, *Thermochim. Acta*, 1986, **104**, 223-245.

34. T. R. Bhat and R. Krishna Iyer, *J. Inorg. Nucl. Chem.*, **1967**, **29**, 179-185.

35. C. Hariharan, *Applied Catalysis A: General*, 2006, **304**, 55-61.

36. X. Tang, E. S. G. Choo, L. Li, J. Ding and J. Xue, *Langmuir*, 2009, **25**, 5271-5275.

37. T. Xia, M. Kovochich, M. Liong, L. Mädler, B. Gilbert, H. Shi, J. I. Yeh, J. I. Zink and A. E. Nel, *ACS Nano*, 2008, **2**, 2121-2134.

38. S.-W. Bian, I. A. Mudunkotuwa, T. Rupasinghe and V. H. Grassian, *Langmuir*, 2011, **27**, 6059-6068.

39. N. M. Franklin, N. J. Rogers, S. C. Apte, G. E. Batley, G. E. Gadd and P. S. Casey, *Environ. Sci. Technol.*, 2007, **41**, 8484-8490.

40. R. Ma, C. Levard, F. M. Michel, G. E. Brown and G. V. Lowry, *Environ. Sci. Technol.*, 2013, **47**, 2527-2534.

41. R. Sitko, E. Turek, B. Zawisza, E. Malicka, E. Talik, J. Heimann, A. Gagor, B. Feist and R. Wrzalik, *Dalton Trans.*, 2013, **42**, 5682-5689.

42. J. P. Gustafsson, **2013**.

43. Z. Wang, A. von dem Bussche, P. K. Kabadi, A. B. Kane and R. H. Hurt, *ACS Nano*, 2013, **7**, 8715-8727.

44. C. Levard, E. M. Hotze, G. V. Lowry and G. E. Brown, *Environ. Sci. Technol.*, 2012, **46**, 6900-6914.

45. J. Liu, D. A. Sonshine, S. Shervani and R. H. Hurt, *ACS Nano*, 2010, **4**, 6903-6913.

46. I. A. Mudunkotuwa, J. M. Pettibone and V. H. Grassian, *Environ. Sci. Technol.*, 2012, **46**, 7001-7010.

47. J. R. Pietruska, X. Liu, A. Smith, K. McNeil, P. Weston, A. Zhitkovich, R. Hurt and A. B. Kane, *Toxicol. Sci.*, 2011, **124**, 138-148.

48. T. Phenrat, T. C. Long, G. V. Lowry and B. Veronesi, *Environ. Sci. Technol.*, 2008, **43**, 195-200.

49. C. Lee, J. Y. Kim, W. I. Lee, K. L. Nelson, J. Yoon and D. L. Sedlak, *Environ. Sci. Technol.*, 2008, **42**, 4927-4933.

50. M. Schriver, W. Regan, W. J. Gannett, A. M. Zaniewski, M. F. Crommie and A. Zettl, *ACS Nano*, 2013, **7**, 5763-5768.

51. F. Zhou, Z. Li, G. J. Shenoy, L. Li and H. Liu, *ACS Nano*, 2013, **7**, 6939-6947.

52. G. Giovannetti, P. Khomyakov, G. Brocks, V. Karpan, J. Van den Brink and P. Kelly, *Phys. Rev. Lett.*, 2008, **101**, 026803.

53. O. Frank, J. Vejpravova, V. Holy, L. Kavan and M. Kalbac, *Carbon*, 2014, **68**, 440-451.

54. L. Wang, Z. Sofer, A. Ambrosi, P. Šimek and M. Pumera, *Electrochem. Commun.*, 2014, **46**, 148-151.

55. M. Pumera, *Electrochem. Commun.*, 2013, **36**, 14-18.

56. J. Liu, Z. Wang, F. D. Liu, A. B. Kane and R. H. Hurt, *ACS Nano*, 2012, **6**, 9887-9899.

57. C.-M. Ho, C.-K. Wong, S. K.-W. Yau, C.-N. Lok and C.-M. Che, *Chemistry – An Asian Journal*, 2011, **6**, 2506-2511.

58. R. D. Kent and P. J. Vikesland, *Environ. Sci. Technol.*, 2011, **46**, 6977-6984.

59. H. Zhang, X. Lv, Y. Li, Y. Wang and J. Li, *ACS Nano*, 2009, **4**, 380-386.

60. Q.-P. Luo, X.-Y. Yu, B.-X. Lei, H.-Y. Chen, D.-B. Kuang and C.-Y. Su, *J. Phys. Chem. C*, 2012, **116**, 8111-8117.

61. Y. Liang, H. Wang, J. Zhou, Y. Li, J. Wang, T. Regier and H. Dai, *J. Am. Chem. Soc.*, 2012, **134**, 3517-3523.

62. S. Guo, D. Wen, Y. Zhai, S. Dong and E. Wang, *ACS Nano*, 2010, **4**, 3959-3968.

63. S. Guo, S. Dong and E. Wang, *ACS Nano*, 2009, **4**, 547-555.

64. R. Reske, H. Mistry, F. Behafarid, B. Roldan Cuenya and P. Strasser, *J. Am. Chem. Soc.*, 2014, **136**, 6978-6986.

65. M. Gattrell, N. Gupta and A. Co, *J. Electroanal. Chem.*, 2006, **594**, 1-19.

66. S. Sen, D. Liu and G. T. R. Palmore, *ACS Catal.*, 2014, **4**, 3091-3095.

67. S. Saha, A. Pal, S. Kundu, S. Basu and T. Pal, *Langmuir*, 2009, **26**, 2885-2893.

68. K. Esumi, R. Isono and T. Yoshimura, *Langmuir*, 2003, **20**, 237-243.

69. S. Wunder, F. Polzer, Y. Lu, Y. Mei and M. Ballauff, *J. Phys. Chem. C*, 2010, **114**, 8814-8820.

70. R. Ciganda, N. Li, C. Deraedt, S. Gatard, P. Zhao, L. Salmon, R. Hernandez, J. Ruiz and D. Astruc, *Chem. Commun. (Cambridge, U. K.)*, 2014, **50**, 10126-10129.

71. R. C. C. Costa, F. C. C. Moura, J. D. Ardisson, J. D. Fabris and R. M. Lago, *Appl. Catal., B*, 2008, **83**, 131-139.

72. R. C. C. Costa, F. C. C. Moura, P. E. F. Oliveira, F. Magalhães, J. D. Ardisson and R. M. Lago, *Chemosphere*, 2010, **78**, 1116-1120.

73. Y. Piao, J. Kim, H. B. Na, D. Kim, J. S. Baek, M. K. Ko, J. H. Lee, M. Shokouhimehr and T. Hyeon, *Nat. Mater.*, 2008, **7**, 242-247.

74. P. Wu, N. Du, H. Zhang, J. Yu and D. Yang, *J. Phys. Chem. C*, 2011, **115**, 3612-3620.

75. S. Kittler, C. Greulich, J. Diendorf, M. Koller and M. Epple, *Chem. Mater.*, 2010, **22**, 4548-4554.

76. A. Kumar, P. K. Vemula, P. M. Ajayan and G. John, *Nat. Mater.*, 2008, **7**, 236-241.

77. Z.-m. Xiu, Q.-b. Zhang, H. L. Puppala, V. L. Colvin and P. J. Alvarez, *Nano Lett.*, 2012, **12**, 4271-4275.

78. X. Yang, A. P. Gondikas, S. M. Marinakos, M. Auffan, J. Liu, H. Hsu-Kim and J. N. Meyer, *Environ. Sci. Technol.*, 2011, **46**, 1119-1127.

79. L. Geranio, M. Heuberger and B. Nowack, *Environ. Sci. Technol.*, 2009, **43**, 8113-8118.

80. J. Dobias and R. Bernier-Latmani, *Environ. Sci. Technol.*, 2013, **47**, 4140-4146.

81. I. V. Lightcap, T. H. Kosel and P. V. Kamat, *Nano Lett.*, 2010, **10**, 577-583.

82. Y. T. Liang, B. K. Vijayan, O. Lyandres, K. A. Gray and M. C. Hersam, *J. Phys. Chem. Lett.*, 2012, **3**, 1760-1765.

83. Q. Xiang, J. Yu, B. Cheng and H. C. Ong, *Chem. - Asian J.*, 2010, **5**, 1466-1474.

84. X. Cao, Z. Yin and H. Zhang, *Energy Environ. Sci.*, 2014, **7**, 1850-1865.